



## Full Length Article

# Numerical and experimental investigation of turbulent *n*-heptane jet-in-hot-coflow flames

Zhiyi Li<sup>a,b,\*</sup>, Michael J. Evans<sup>c</sup>, Jingjing Ye<sup>c</sup>, Paul R. Medwell<sup>c</sup>, Alessandro Parente<sup>a,b,\*</sup>

<sup>a</sup> Université Libre de Bruxelles, Ecole polytechnique de Bruxelles, Aero-Thermo-Mechanics Laboratory, Brussels, Belgium

<sup>b</sup> Université Libre de Bruxelles and Vrije Universiteit Brussel, Combustion and Robust Optimization Group (BURN), Brussels, Belgium

<sup>c</sup> The University of Adelaide, School of Mechanical Engineering, Adelaide, Australia

## ARTICLE INFO

## Keywords:

*n*-heptane  
Turbulent flames  
Partially-stirred reactor (PaSR)  
Jet-in-hot-coflow (JHC) burner  
MILD combustion  
URANS simulation

## ABSTRACT

A turbulent *n*-heptane jet flame in a jet-in-hot-coflow burner is numerically and experimentally investigated, revealing distinct features of this fuel in a jet-in-hot-coflow burner. The RANS *k*- $\epsilon$  turbulence model is adopted in combination with a dynamic partially-stirred reactor (PaSR) combustion model. The simulation results are used to support newly-obtained experimental measurements of mean temperature, OH number density and normalised CH<sub>2</sub>O-PLIF signal values at several axial locations. The simulations capture the transitional phenomenon observed experimentally for the low coflow oxygen concentration case, which is determined to be due to the two chemical pathways which exist for the *n*-heptane fuel. The predicted flame weak-to-strong transition heights based on the streamwise (axial) gradient of OH number density show non-monotonic behaviour. Furthermore, an investigation on negative heat release rate region shows that the absolute value of negative heat release rate increases with reduced coflow oxygen content, in contrast to the suppression phenomenon seen in laminar opposed-flow flames.

## 1. Introduction

Novel combustion technologies with low emissions, high efficiency and fuel flexibility have become essential to cope with the energy supply challenge the world will face in the near future. One such technology is termed Moderate or Intense Low-oxygen Dilution (MILD) combustion [1–3]. In industrial applications, MILD combustion is often achieved by means of high velocity burners and flue gas recirculation coupled with high level of excess air and/or intense heat extraction [4]. The resultant pre-heated and highly-diluted mixture helps to stabilize and homogenize the flame, thus reducing combustion noise [1]. Dilution also impacts the system reactivity, leading to a distributed oxidation process. As a result, a more uniform temperature field is obtained and thermal NO<sub>x</sub> production is largely suppressed [1,2].

For research purposes, jet-in-hot-coflow (JHC) burners [5–8] are often used to produce pre-heated and highly-diluted conditions to reach MILD combustion regime, decreasing the geometrical complexity and allowing the use of sophisticated measurement techniques. Several investigations have focused on the JHC burners, both experimentally and numerically [6,9,10,5,11–13,4,14]. JHC burners feature a central jet and a secondary burner providing hot exhaust products as a coflow, thus emulating the effect of flue gas recirculation. Dally et al. [6]

carried out experiments with an equimolar fuel jet of CH<sub>4</sub>/H<sub>2</sub>, at different oxygen levels (9%, 6% and 3% by mass) in the hot coflow. They concluded that the peak temperature increase in the reaction zone can be as low as 100 K, by reducing the oxygen level to 3%; and the production of CO, NO and OH is largely reduced when compared with conventional combustion conditions. At the same time, they provided high-fidelity mean and RMS (root-mean-square) experimental data of temperature and various chemical species for numerical validation. Formaldehyde (CH<sub>2</sub>O) has been identified as an important precursor in controlling the initiation of reaction in methane flames, as explained by Gordon et al. [15]. Medwell et al. [16,9] used planar laser-induced fluorescence (PLIF) and Rayleigh scattering techniques to reveal the distribution of formaldehyde (CH<sub>2</sub>O), hydroxyl radical (OH), and temperature under the influences of hydrogen addition. They indicated that the reaction zone was not very sensitive to hydrogen addition, showing the potential of MILD combustion for fuel flexibility. They also observed a “lift-off” height based on the weak-to-strong transition of OH and the existence of a pre-ignition region in the apparent lifted region of these flames [16].

Experimental investigations on JHC burners have mostly focused on gaseous, simple hydrocarbon fuels. However, a few studies [17,18,8,19–22] focused on the behaviour of pre-vaporized oxygenated

\* Corresponding authors.

E-mail addresses: [z1443@cam.ac.uk](mailto:z1443@cam.ac.uk) (Z. Li), [Alessandro.Parente@ulb.ac.be](mailto:Alessandro.Parente@ulb.ac.be) (A. Parente).

<https://doi.org/10.1016/j.fuel.2020.118748>

Received 21 November 2019; Received in revised form 13 July 2020; Accepted 15 July 2020

Available online 13 August 2020

0016-2361/ © 2020 Elsevier Ltd. All rights reserved.

fuels and long-chain alkanes. Despite the high flexibility about the fuel choice in MILD combustion [23], systems with more complex fuels could lead to distinct features [24–26]. Therefore, Ye et al. [8] performed experimental investigations with *n*-heptane fuel using conventional photography and PLIF, finding that the “lift-off” height (weak-to-strong transition height) changes monotonically with decreasing coflow oxygen level—this does not occur for other simple hydrocarbon fuels. In the transition from conventional lifted flame to MILD combustion, the sharp rise of temperature disappears, leading to gradually increased OH levels upstream like a tail [27]. When the dilution level reaches fully MILD condition, the OH tail is attached to the jet exit plane, as reported by [28]. However, in *n*-heptane flames, the transitional flame structure is still observed for a much lower coflow oxygen content [8], compared to simple fuels. Based on the analysis of fuel pyrolysis and heat release with *n*-heptane and ethanol, they concluded that it is more difficult to establish MILD conditions with *n*-heptane [8].

As a result of the reduced reactivity under highly-diluted conditions, the chemical timescales increase and the strong interaction between chemistry reaction and mixing makes the modelling of such flames more challenging than conventional ones. Numerical investigations of JHC-type burners have been carried out using Reynolds-Averaged Navier–Stokes (RANS) simulations [29–33,4,10,34–37,14,38], Large Eddy Simulations (LES) [13,39–42] and Direct Numerical Simulations (DNS) [43]. Simple fuels such as methane, hydrogen and ethylene have been the main focus. The experimental and numerical studies on JHC burner under MILD condition with simple fuels have revealed some common signatures, such as the absence of the negative heat release rate region, the broadening of the heat production profile with a single peak in mixture fraction space and the suppression of the pyrolytic reactions [44,3]. However, using complex fuels such as oxygenated hydrocarbons and long-chain alkanes under highly-diluted conditions in order to reach MILD combustion regime has shown distinct features, like the appearance of visible flames and increased pollutant emissions [25,45,46].

The relevance of finite-rate chemistry effect in the jet-in-hot-coflow flames makes the use of models based on the principle of timescale separation challenging [47]. Therefore, models implementing detailed chemical mechanisms should be considered. Among them, the eddy dissipation concept (EDC) [48–50] and the Partially Stirred Reactor (PaSR) [51] models represent a viable choice, as they allow inclusion of detailed chemistry in a computationally-affordable way. Compared to the models based on scale separation like the flamelet model [52] and eddy dissipation model (EDM) [53], the finite-rate based models (EDC and PaSR) solve transport equations of each chemical species and integrate the ordinary differential equations (ODEs) of the chemical source terms. The EDC and PaSR model split each computational cell into two regions: the reactive structures, where reactions take place, and the surrounding fluid, where mixing happens. In PaSR, the interaction between turbulence and chemistry is represented with a factor  $\kappa$  [51], which is defined as the ratio between the chemical timescale and the sum of mixing and chemical scales. In EDC, a similar parameter is adopted:  $\gamma$  [48–50], whose definition depends solely on turbulence parameters, through an energy cascade model [48–50]. In PaSR, both the chemical and mixing timescales are included in the estimation of the splitting fraction explicitly, allowing a more accurate description on turbulence/chemistry interactions. Recently, an extension of the PaSR model has been proposed, based on the dynamic estimation of the mixing timescale, showing improved predictions for the simulation of the JHC burner [54,55]. Therefore, the dynamic PaSR model is adopted in the present paper.

The jet-in-hot-coflow *n*-heptane flames have been studied through experimental measurement and laminar calculations [8]. However, the chemical complexity involved in the problem makes the selected case a quite challenging one. Previous work by Ye et al. [8] is a phenomenological study of JHC flames with different fuels, including the complex ones. The purpose of the current article is to investigate the role of

turbulence-chemistry interactions in *n*-heptane flames and to support the experimental investigation quantitatively with CFD simulations, looking at newly obtained experimental data—mean temperature and semi-quantitative species measurements, viz. OH number density values and normalized CH<sub>2</sub>O-PLIF signals as validation targets.

Simulations were carried out using the dynamic PaSR combustion model, in combination with detailed kinetic mechanisms of *n*-heptane with more than 100 species and about 2,000 reactions. Because of the intense turbulence-chemistry interactions under MILD regime, the Unsteady Reynolds Averaged Navier–Stokes (URANS) approach was used to capture complex phenomena such as local extinction and re-ignition. Taking the complexity of the chemical mechanism chosen into account, this option was preferred over the use of Large Eddy Simulation (LES). The influence of turbulence modelling on the results is first reported, to identify optimised settings for the subsequent simulations focusing on turbulence-chemistry interactions. The investigation of the chemical timescale distribution, flame weak-to-strong transition height and negative heat release rate are presented as well, to identify the key features of the investigated *n*-heptane flames.

## 2. Mathematical models

### 2.1. Turbulence model

The density-based Favre-averaged (marked with  $\sim$ ) governing equations of mass, momentum and energy [56] are solved using the URANS approach:

$$\frac{\partial \bar{\rho}}{\partial t} + \frac{\partial}{\partial x_j} (\bar{\rho} \tilde{u}_j) = 0, \quad (1)$$

$$\frac{\partial}{\partial t} (\bar{\rho} \tilde{u}_i) + \frac{\partial}{\partial x_j} (\bar{\rho} \tilde{u}_i \tilde{u}_j) = -\frac{\partial \bar{p}}{\partial x_i} + \frac{\partial}{\partial x_j} (\bar{\tau}_{ij} - \bar{\rho} \tilde{u}_i \tilde{u}_j''), \quad (2)$$

$$\frac{\partial}{\partial t} (\bar{\rho} \tilde{h}) + \frac{\partial}{\partial x_j} (\bar{\rho} \tilde{h} \tilde{u}_j) = \frac{\partial}{\partial x_j} \left( \bar{\rho} \alpha \frac{\partial \tilde{h}}{\partial x_j} - \bar{\rho} \tilde{u}_j \tilde{h}'' \right) - \frac{\partial}{\partial x_j} (\bar{q}_{r,j}) + \bar{S}_{hc}, \quad (3)$$

where  $\rho$ ,  $u$  and  $p$  represent the density, velocity and pressure respectively; the sensible enthalpy is denoted with  $h$ ;  $\alpha$  is the thermal diffusivity. The term  $q_r$  denotes the radiative heat loss and  $S_{hc}$  represents the heat production from chemical reaction. The turbulent heat flux  $-\bar{\rho} \tilde{u}_j \tilde{h}''$  is modelled with:

$$-\bar{\rho} \tilde{u}_j \tilde{h}'' \approx \frac{\mu_t}{Pr_t} \frac{\partial \tilde{h}}{\partial x_j}, \quad (4)$$

where the turbulent Prandtl number is set to  $Pr_t = 0.85$  and  $\mu_t$  is the turbulent (eddy) viscosity.

The Favre-averaged transport equation of reactive scalar  $Y_s$  reads:

$$\frac{\partial}{\partial t} (\bar{\rho} \tilde{Y}_s) + \frac{\partial}{\partial x_j} (\bar{\rho} \tilde{Y}_s \tilde{u}_j) = \frac{\partial}{\partial x_j} \left( \left( D_s + \frac{\mu_t}{Sc_t} \right) \frac{\partial \tilde{Y}_s}{\partial x_j} \right) + \bar{\omega}_s, \quad (5)$$

in which  $D_s$  is the molecular diffusivity and  $Sc_t$  denotes the turbulent Schmidt number, representing the ratio between turbulent viscosity and turbulent diffusivity  $D_t$ ; and  $\bar{\omega}_s$  is the chemical source term. The choice of the turbulent Schmidt number strongly impacts the temperature and species distribution.

The standard  $k$ - $\epsilon$  turbulence model is used. The unresolved turbulence stresses  $\bar{\rho} \tilde{u}_i \tilde{u}_j''$  are modelled with the product of an eddy viscosity  $\mu_t$  and mean flow strain rate  $S_{ij}$ . Finally, the eddy viscosity  $\mu_t$  in standard  $k$ - $\epsilon$  model is estimated as:

$$\mu_t = \rho C_\mu \frac{\tilde{k}^2}{\tilde{\epsilon}}. \quad (6)$$

In Eq. (6), the constant  $C_\mu$  equals 0.09. The Favre-averaged turbulence kinetic energy  $\tilde{k}$  and the dissipation rate  $\tilde{\epsilon}$  of the turbulence kinetic energy are solved via two separate transport equations [56]:

$$\frac{\partial}{\partial t}(\bar{\rho}\tilde{k}) + \frac{\partial}{\partial x_j}(\bar{\rho}\tilde{k}\tilde{u}_j) = \frac{\partial}{\partial x_j} \left( \left( \mu + \frac{\mu_t}{\sigma_k} \right) \frac{\partial \tilde{k}}{\partial x_j} \right) + 2\mu_t E_{ij} E_{ij} - \bar{\rho}\tilde{\epsilon}, \quad (7)$$

$$\begin{aligned} \frac{\partial}{\partial t}(\bar{\rho}\tilde{\epsilon}) + \frac{\partial}{\partial x_j}(\bar{\rho}\tilde{\epsilon}\tilde{u}_j) \\ = \frac{\partial}{\partial x_j} \left( \left( \mu + \frac{\mu_t}{\sigma_\epsilon} \right) \frac{\partial \tilde{\epsilon}}{\partial x_j} \right) + C_{\epsilon 1} \bar{\rho} \frac{\tilde{\epsilon}}{k} 2\mu_t E_{ij} E_{ij} - C_{\epsilon 2} \bar{\rho} \frac{\tilde{\epsilon}^2}{k}, \end{aligned} \quad (8)$$

in which  $E_{ij}$  represents the mean rate of deformation with

$$E_{ij} = \frac{1}{2} \left[ \frac{\partial u_i}{\partial x_j} + \frac{\partial u_j}{\partial x_i} \right]; \quad (9)$$

$\sigma_k$ ,  $\sigma_\epsilon$ ,  $C_{\epsilon 1}$  and  $C_{\epsilon 2}$  are model constants, set by default to 1.0, 1.30, 1.45 and 1.90, respectively [57]. The standard  $k$ - $\epsilon$  model is robust, computationally fast and has the potential advantage of generality since it requires no direct empirical input such as a mixing-length specification. However, it has the well-known disadvantage of over-estimating the jet spread rate for axisymmetric jets [57]. To correct that, some model modifications have been proposed. Whilst changing the  $C_{\epsilon 1}$  to 1.6 helps reducing the jet-decay over-estimation [57,31,4], such a modification lacks generality. Pope [57] suggested a correction and a further development of the standard  $k$ - $\epsilon$  model, adding an additional term to the kinetic energy dissipation rate transport equation:

$$S_{\epsilon_{\text{Pope}}} = C_{\epsilon 3} \frac{\tilde{\epsilon}^2}{k} \psi, \quad (10)$$

where  $\psi = \omega_{ij} \omega_{jk} S_{ki}$  measures the vortex stretching.  $\omega_{ij}$  and  $S_{ki}$  are defined as

$$\omega_{ij} = \frac{1}{2} \frac{\tilde{k}}{\tilde{\epsilon}} \left( \frac{\partial \tilde{u}_i}{\partial x_j} - \frac{\partial \tilde{u}_j}{\partial x_i} \right), \quad (11)$$

and

$$S_{ki} = \frac{1}{2} \frac{\tilde{k}}{\tilde{\epsilon}} \left( \frac{\partial \tilde{u}_i}{\partial x_j} + \frac{\partial \tilde{u}_j}{\partial x_i} \right), \quad (12)$$

respectively.

Qualitative considerations indicate that the source of dissipation is a linearly increasing function of  $\psi$  [57]. Thus, the term  $C_{\epsilon 3} \frac{\tilde{\epsilon}^2}{k} \psi$  is added in the transport equation of the kinetic energy dissipation rate (Eq. (8)) to improve the generality of the  $k$ - $\epsilon$  model. The impact of the choice of the turbulent Schmidt number and of the turbulence model is discussed in Section 4.

## 2.2. Combustion model—PaSR model

The PaSR model [51,58], assumes that each computational cell is separated into two zones: one where reactions take place, and another characterized by mixing alone. Turbulence drives the exchange between the two zones. The final species concentration of the cell is the weighted mean value between the reactive zone and the mixing zone. A conceptual drawing of the PaSR model is shown in Fig. 1.

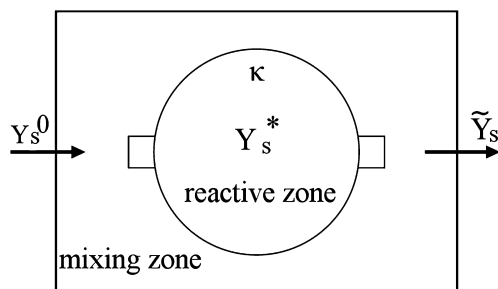


Fig. 1. Conceptual drawing of the PaSR model (adapted from Li et al. [38]).

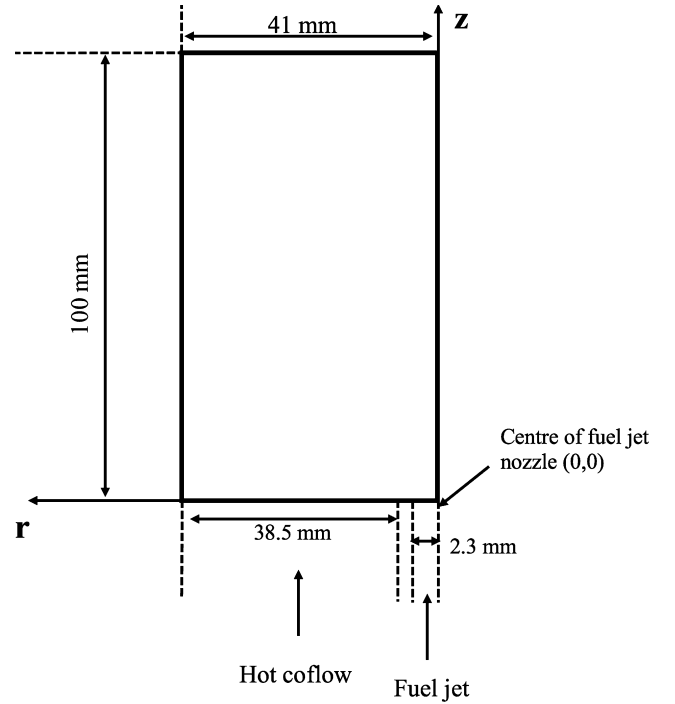


Fig. 2. Two-dimensional schematic of the JHC burner.

Fig. 2 depicts one computational cell, in which  $Y_s^0$  is the initial  $s_{th}$  species mass fraction in the non-reactive region,  $\tilde{Y}_s$  is the final averaged  $s_{th}$  species mass fraction in the cell and  $Y_{s^*}$  is the  $s_{th}$  species mass fraction in the reactive zone. The term  $\kappa$  is the mass fraction of the reactive zone in the cell, which is estimated with [59]:

$$\kappa = \frac{\tau_c}{\tau_c + \tau_{mix}}, \quad (13)$$

where  $\tau_c$  and  $\tau_{mix}$  are the characteristic chemical and mixing timescales, respectively. The complexity of the model lies, therefore, in the estimation of  $\tau_c$  and  $\tau_{mix}$ , as described in previous publications [54,38].

In the present work, the mixing timescale is evaluated with a dynamic approach [54,38]—as the ratio of the scalar variance,  $\tilde{\phi}^{n^2}$ , and the scalar dissipation rate,  $\tilde{\epsilon}_\phi$  [60]:

$$\tau_{mixDynamic} = \frac{\tilde{\phi}^{n^2}}{\tilde{\epsilon}_\phi}. \quad (14)$$

The mixture fraction  $Z$  is selected to describe the mixing process of a scalar. Therefore, the scalar variance and dissipation rate take the form of the mixture fraction variance ( $\tilde{Z}^{n^2}$ ) and mixture fraction dissipation rate ( $\tilde{\chi}$ ). They are obtained by solving the following transport equations [61,62]:

$$\frac{\partial \bar{\rho}\tilde{Z}}{\partial t} + \frac{\partial \bar{\rho}\tilde{u}_j\tilde{Z}}{\partial x_j} = \frac{\partial}{\partial x_j} \left( \bar{\rho} \left( D_s + D_t \right) \frac{\partial \tilde{Z}}{\partial x_j} \right), \quad (15)$$

$$\frac{\partial \bar{\rho}\tilde{Z}^{n^2}}{\partial t} + \frac{\partial \bar{\rho}\tilde{u}_j\tilde{Z}^{n^2}}{\partial x_j} = \frac{\partial}{\partial x_j} \left( \bar{\rho} \left( D_s + D_t \right) \frac{\partial \tilde{Z}^{n^2}}{\partial x_j} \right) + 2\rho D_t \left( \frac{\partial \tilde{Z}}{\partial x_j} \right)^2 - \bar{\rho}\tilde{\chi}, \quad (16)$$

$$\begin{aligned} \frac{\partial \bar{\rho}\tilde{\chi}}{\partial t} + \frac{\partial \bar{\rho}\tilde{u}_j\tilde{\chi}}{\partial x_j} = \frac{\partial}{\partial x_j} \left( \bar{\rho} \left( D_s + D_t \right) \frac{\partial \tilde{\chi}}{\partial x_j} \right) - C_1 \bar{\rho} \frac{\tilde{\chi}^2}{Z^{n^2}} \\ - C_2 \bar{\rho}^2 \frac{C_\mu \tilde{k}}{\mu_t} \tilde{\chi} + C_3 \frac{\bar{\rho} C_\mu \tilde{k}}{S_{ct}} \left( \frac{\partial \tilde{Z}}{\partial x_j} \right)^2 + C_4 \mu_t \frac{\tilde{\chi}}{\tilde{k}} \left| \tilde{S} \right|^2. \end{aligned} \quad (17)$$

In the present work, the molecular diffusivity  $D$  is estimated with

thermal diffusivity  $\alpha$ , given the absence of species such as  $H_2$ . The turbulent diffusivity is calculated using  $D_t = \mu_t/(\rho Sc_t)$ . In Eqn. 17,  $C_1, C_2, C_3$  and  $C_4$  are model constants. They are set to  $C_1 = 1.0, C_2 = 1.8, C_3 = 1.7$  and  $C_4 = 1.4$  [61] in the current study.

The chemical timescale can be obtained from the Jacobian matrix ( $J$ ) of the chemical source terms [63,64]. The decomposition of the source term Jacobian matrix is accurate but time consuming, especially when a large mechanism is used. As an alternative, the formation rates can be used. The chemical timescale of each chemical species can be approximated with the ratio of the species mass fraction and formation rate in the reactive structure [65,14]:

$$\tau_{c,s} = \frac{Y_{*s}}{|dY_{*s}/dt|}. \quad (18)$$

After removing the dormant species (characterised by a formation rate smaller than  $10^{-16}s^{-1}$ , the slowest chemical time is chosen as the characteristic chemical timescale.

$$\tau_c = \max(\tau_{c,s}). \quad (19)$$

The threshold species formation rate cannot be too large, otherwise the minor species which are important to the chemical reaction will be left out. At the same time, it cannot be too small, so that the dormant species with very low formation rates can be excluded. After a sensitivity analysis spanning 6 decades from  $10^{-10}s^{-1}$  to  $10^{-16}s^{-1}$ , the value of  $10^{-16}s^{-1}$  is chosen as the threshold to define the dormant species. As smaller values are not found to affect the determination of chemical time scale. A detailed discussion about the choice of the threshold is reported in the [Supplementary material](#).

Finally, the mean source term  $\bar{\omega}_s$  in the species transport equation is expressed as:

$$\bar{\omega}_s = \kappa \frac{\tilde{\rho}(Y_{*s} - Y_s^0)}{\tau^*}, \quad (20)$$

where  $\tau^*$  is the residence time in the reactive structure. In the present work, the mixing timescale is used as the residence time  $\tau^*$ . Indeed, the characteristic residence time in the reacting fraction should not only be based on the mixing time scale, but also accounting for the characteristic chemical time scale. For the current investigated system, the chemical time scale is always larger than the mixing time scale, indicating that the characteristic residence time can be estimated using the mixing time, as shown in the [Supplementary material](#). A canonical reactor is solved to obtain the value of  $Y_{*s}$ . The reactive zone is modelled as an ideal reactor evolving from the initial value of  $Y_s^0$ :

$$\frac{dY_{*s}}{dt} = \frac{\dot{\omega}_s}{\rho}. \quad (21)$$

The term  $\dot{\omega}_s$  represents the instantaneous formation rate of species  $s$ . The final integration of  $\frac{dY_{*s}}{dt}$  over the residence time of  $\tau^*$  is  $Y_{*s}$ . In the PaSR model, the intensity of turbulence-chemistry interactions are quantified by the factor  $\kappa$ , defining the fraction of the reactive structure in the cell, which is directly affected by the values of the chemical and mixing time scales. In other words, any change in  $\tau_c$  and  $\tau_{mix}$  will directly lead to the change of source terms.

### 3. Methodology

#### 3.1. Experimental approach

The experimental validation data are newly obtained and presented here for the first time. These experimental data complement those reported by Ye et al. [8], undertaken in the same JHC burner using  $n$ -heptane as fuel. The JHC burner used in this study has a cooled central jet with the inner diameter of  $D = 4.6$  mm [8]. The liquid  $n$ -heptane fuel is mixed with carrier air and then preheated by a controlled evaporator and mixer (CEM). The temperature of the mixture at the central jet exit plane is 412 K, which is higher than the  $n$ -heptane boiling point

**Table 1**  
Jet and coflow characteristics.

Profiles	Central jet	Hot coflow
Velocity	50 m/s	2.4 m/s
Temperature	412 K	1250 K
Reynolds number	10,000	1000

**Table 2**  
Species mass fractions from equilibrium calculation.

Species	$nC_7H_{16}$	$O_2$	$N_2$	$H_2O$	$CO_2$	OH
Fuel stream	0.398	0.462	0.140	0	0	0
Coflow 3%	0	0.0347	0.8382	0.0697	0.0573	$2.27 \times 10^{-06}$
Coflow 6%	0	0.0703	0.8034	0.0693	0.0570	$2.68 \times 10^{-06}$
Coflow 9%	0	0.1045	0.7696	0.0691	0.0568	$2.96 \times 10^{-06}$

(371 K). A secondary burner located 90 mm upstream of the exit plane has an inner diameter of 82 mm. The secondary burner produces the hot combustion products from a lean mixture of natural gas, hydrogen, air and nitrogen. Changing the ratios of these gases allows the coflow oxygen level and temperature to be varied independently. The mean gas temperature, mean velocity and Reynolds number of the central jet and hot coflow are reported in [Table 1](#). The equilibrium composition for species of  $O_2, N_2, H_2O, CO_2$  and OH obtained from equilibrium calculations with coflow adiabatic temperature are provided in [Table 2](#).

The mean and RMS values of temperature and species are measured using the optical techniques of Rayleigh scattering and planar laser-induced fluorescence (PLIF) [8,20]. Temperature, semi-quantified number density of OH as well as the normalized  $CH_2O$ -PLIF signal are reported at the axial locations of 14.5 mm (3.2D), 22.5 mm (4.9D), 29.5 mm (6.4D), and 59.5 mm (12.9D). The  $CH_2O$ -PLIF signal is not quantified due to challenges with determining the quenching rates. The uncertainty in the species profiles is the principle source of uncertainty for the Rayleigh scattering and can be estimated as smaller than 2% [66]. The typical uncertainty in the temperature data in the coflow and reaction zone varies from 5% to 10% [20,67,15].

#### 3.2. Numerical configuration

[Fig. 1](#) presents a two-dimensional schematic of the axisymmetric domain. The axial direction is denoted with  $z$ , and the radial direction marked with  $r$ . The bulk mean velocities used for the jet and coflow streams are given in [Table 1](#), with corresponding Reynolds numbers, and compositions are given in [Table 2](#).

A two-dimensional structured mesh is used in the simulation after a mesh sensitivity analysis. The mesh sensitivity analysis is included in the [Supplementary material](#). The mesh has 4450 hexahedral cells and 100 prisms. A pre-inlet with the length of 100 mm including the burner wall is used. The computational domain extends 100 mm further downstream. Only the fuel jet and hot coflow streams are considered in the simulation, since the experimental data are available up to 59.5 mm downstream of the jet outlet, and mixing with fresh air from the surroundings (quiescent air) only has an effect from 100 mm above the jet exit plane [8].

Because the turbulent Schmidt number  $Sc_t$  is varied according to the specific flow nature, there is no universally-accepted formulation in the literature [68]. Furthermore, it is also indicated [41] that the optimal range of  $Sc_t$  is broad (from 0.2 to 1.5 for jet flows). Therefore, a sensitivity study to the choice of the turbulent Schmidt number is first presented, setting the  $Sc_t$  to 0.7, 1.0, 1.2 and 1.3. The Pope correction [57] is used here in combination with the standard  $k-\epsilon$  turbulence model, to correct the spreading rate of the jet. The PaSR combustion model with the dynamic calculation of mixing timescale is adopted. The temperature, velocity and species mass fractions from [Tables 1 and 2](#)

are used as boundary conditions. The mass fractions for the species of  $O_2$ ,  $N_2$ ,  $H_2O$ ,  $CO_2$  and  $OH$  are provided for the hot coflow boundary, because the hot coflow is produced by a premixed  $CH_4/H_2/N_2$ /air flame. Furthermore, the species included in the hot coflow boundary have equilibrium concentrations greater than 1 ppm by volume (*viz.*  $O_2$ ,  $N_2$ ,  $CO_2$ ,  $H_2O$ ,  $OH$ ). Medwell et al. [69,70] and Evans et al. [71] noted the significant effects of minor species (going down to 0.1 ppb) on premixed reactors. However, trace species (for example,  $O$ ,  $H$ ,  $CH_2O$ ) are significantly less important with volume fraction lower than 10 ppm and they have previously been shown to not have a significant effect in the RANS simulations of jet-in-hot-coflow flames [71,10]. Therefore, such species are not included in the boundary conditions. A reduced *n*-heptane mechanism with 106 species and 1738 reactions [72–74] was used for most simulations. Numerical results using a detailed mechanism with 654 species and 2827 reactions [75,76] showed minor differences when compared with the results provided by the reduced one and they are presented in the [Supplementary material](#).

## 4. Results and discussion

### 4.1. Turbulence model parameters

The influence of the turbulent Schmidt number on the mean temperature and  $OH$  distribution is presented in [Figs. 3–5](#), for each of the three coflow  $O_2$  levels considered. The temperature in the fuel jet is not measured, therefore the experimental temperature values close to the centerline at axial locations of 14.5, 22.5 and 29.5 mm are not available. It should be also noted that the apparent  $OH$  signal along the jet centerline is an artefact of interference from fuel Raman and is not indicative of  $OH$ . Importantly, this interference only affects very near the centerline, as apparent by the rapid decrease with radial distance—this interference does not affect the location or value of the peak  $OH$  concentration.

[Fig. 3](#) shows that using a turbulent Schmidt number  $Sc_t = 0.7$  results in early ignition of the jet flame for the case with coflow oxygen level of 9%. A generalized over-prediction of mean temperature profiles is observed at axial locations  $z = 22.5, 29.5$  and  $59.5$  mm. The location of peak temperature is shifted slightly to the right (away from the centerline) for  $z = 59.5$  mm. Furthermore, the region with temperature above that of the coflow temperature (1250 K) is broader than observed experimentally. On the other hand, using  $Sc_t = 1.3$  leads to a 140 K under-prediction of the mean temperature at  $z = 59.5$  mm. Low turbulent Schmidt numbers increase the scalar diffusivity (see [Eq. \(5\)](#)), leading to enhanced mixing between the fuel and oxidizer species, thus

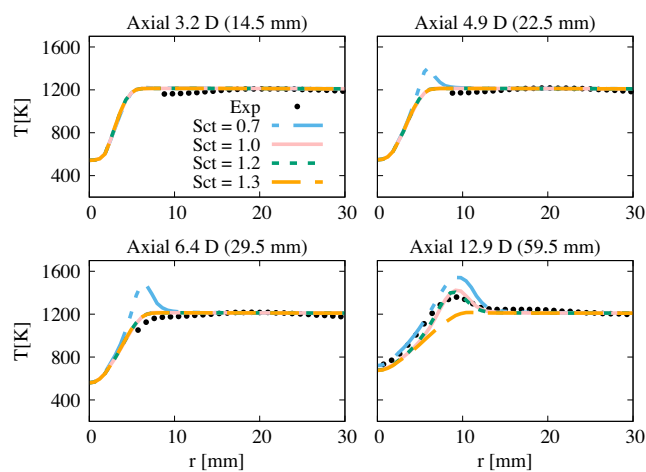


**Fig. 3.** Mean temperature profiles obtained with various turbulent Schmidt numbers (0.7, 1.0, 1.2 and 1.3), compared with the experimental data at several axial locations. Coflow oxygen level of 9%.

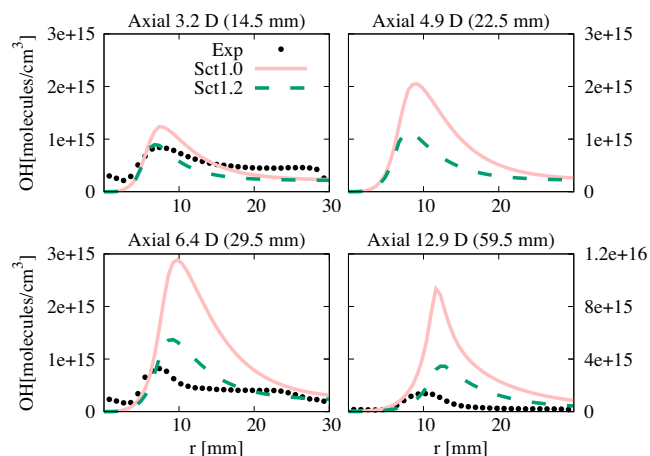


**Fig. 4.** Mean experimental and numerical  $OH$  number density profiles at several axial locations. Coflow oxygen level of 3%. The scale used at  $z = 59.5$  mm is different from the one used at the other locations.

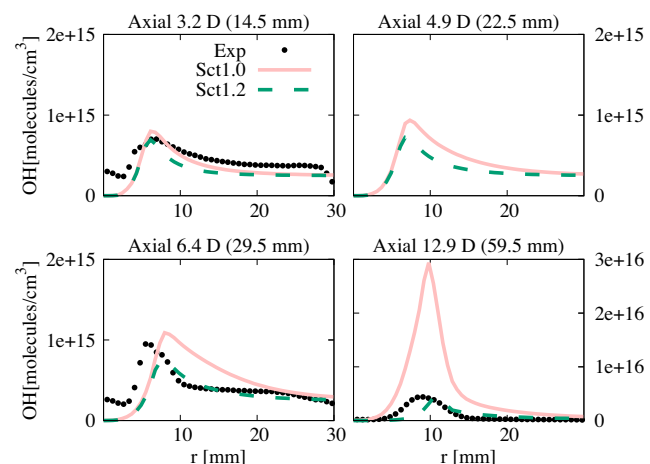


**Fig. 5.** Mean experimental and numerical  $OH$  number density profiles at several axial locations. Coflow oxygen level of 6%. The scale used at  $z = 59.5$  mm is different from the one used at the other locations.

promoting chemical reactions. However, high turbulent Schmidt number influences the flow in the opposite way; as a result, the flame ignition is delayed. Setting  $Sc_t$  to 1.0 or 1.2 provides satisfactory mean temperature predictions.

The differences between choosing  $Sc_t = 1.0$  and  $Sc_t = 1.2$  is revealed through the  $OH$  distributions in coflows with oxygen levels of 3% and 6% (shown in [Fig. 4 and 5](#)). The scale used for the locations of  $z = 14.5, 22.5$  and  $29.5$  mm is different from the one used for  $z = 59.5$  mm. No experimental data are available at  $z = 22.5$  mm for 3% and 6%  $O_2$  cases—the numerical values are shown as a comparison with the 9% case. Since the  $OH$  number density (molecules/cm<sup>3</sup>) is measured experimentally, the mole fractions of  $OH$  are extracted from the simulations and converted for direct comparison. At locations far from the centerline ( $r \geq 15$  mm), the predicted  $OH$  level is close to the experimental value with both  $Sc_t = 1.0$  and  $Sc_t = 1.2$ . However, the calculated  $OH$  peaks at  $z = 14.5, 29.5$  and  $59.5$  mm are higher than the experimental data when  $Sc_t = 1.0$  is chosen. Particularly at  $z = 59.5$  mm, where  $OH$  is over-predicted by more than six times. Choosing  $Sc_t = 1.2$  keeps the  $OH$  peak value closer to the experimental data for both the 3% and 6% cases, especially at  $z = 14.5$  mm. At  $z = 59.5$  mm, using  $Sc_t = 1.2$  still over-predicts  $OH$  for the coflow oxygen level of 3%, although significantly less than with  $Sc_t = 1.0$ . Based on this analysis, a turbulent Schmidt number of 1.2 was chosen for the remainder of the simulations.

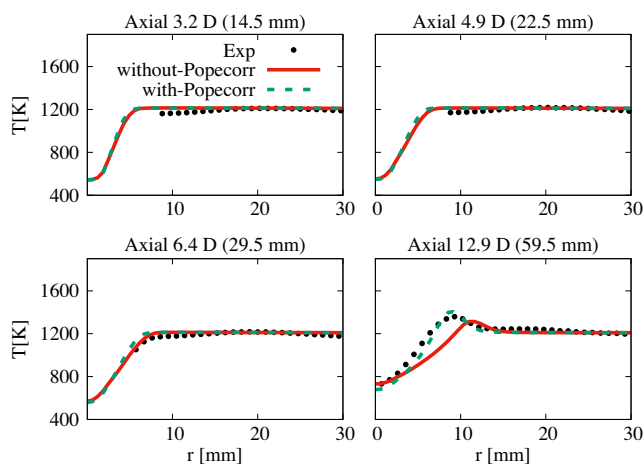


Fig. 6. Mean temperature profiles obtained with and without Pope correction, compared with the experimental data at several axial locations. Coflow oxygen level of 9%.

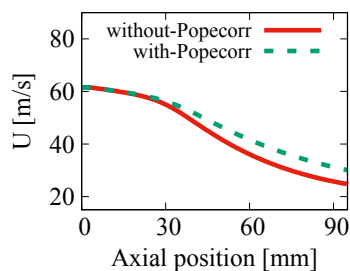


Fig. 7. Mean velocity profile on the centerline obtained with and without Pope correction. Coflow oxygen level of 9%.

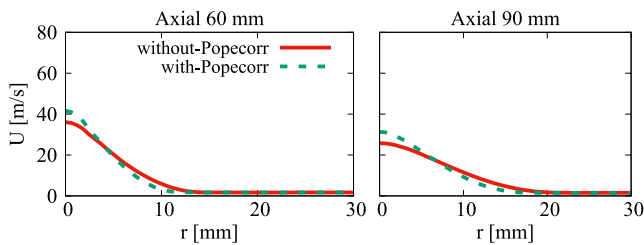


Fig. 8. Mean velocity profile at 60 mm and 90 mm axial locations, obtained with and without Pope correction. Coflow oxygen level of 9%.

Adoption of the Pope correction has major influence on the flow field of the jet. Fig. 6 shows the mean temperature profiles for the 9%  $O_2$  case, with and without the Pope correction. Very similar predicted profiles are obtained at  $z = 14.5/22.5/29.5$  mm. At  $z = 59.5$  mm, the standard  $k-\varepsilon$  model fails to predict the peak temperature location correctly, while results with the Pope correction closely follow the experimental profile. Comparing the jet decay on the centerline in Fig. 7, a faster jet decay is featured after  $z = 30$  mm if no Pope correction is used. Moreover, Fig. 8 indicates that the spread rate is higher without Pope correction, which shifts the stoichiometric mixture location further away from the centerline. Ultimately, the combination of  $Sc_t = 1.2$  and Pope correction is chosen in the current study.

#### 4.2. The influence of oxygen level

Fig. 6 shows that the mean temperature profiles for the 9% case are very well predicted with the turbulent and combustion models chosen. The predicted temperature profiles obtained for the 3%  $O_2$  and 6%  $O_2$  cases are compared to the available experimental measurements in

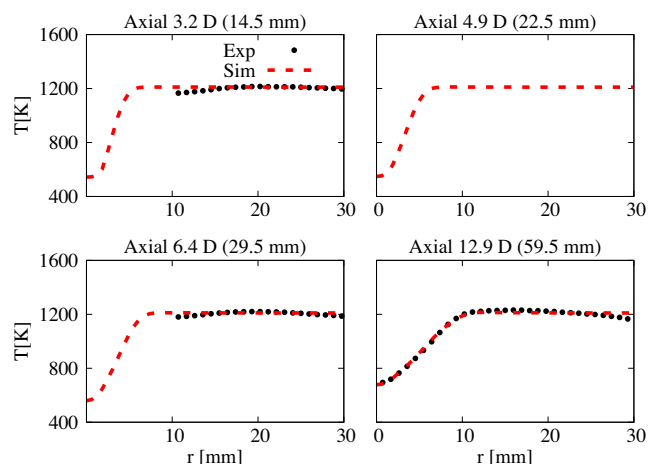


Fig. 9. Mean experimental and numerical temperature profiles, at different axial locations. Coflow oxygen level of 3%.

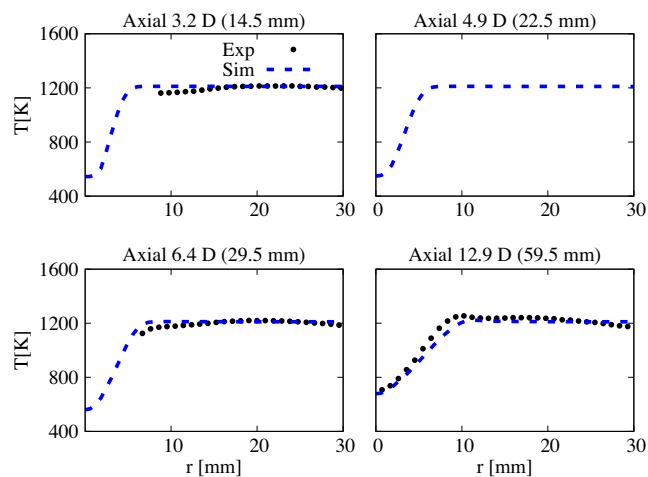


Fig. 10. Mean experimental and numerical temperature profiles, at different axial locations. Coflow oxygen level of 6%.

Fig. 9 and Fig. 10. The 3%  $O_2$  and 6%  $O_2$  cases show peak temperature at  $z = 59.5$  mm of about 1230 K and 1240 K, respectively, thus more than 100 K lower than the maximum measured temperature for 9%  $O_2$  (around 1360 K) case. The numerical model can capture the temperature levels quite well, showing remarkable agreement with the measured data. As previously indicated, no experimental data are available at  $z = 22.5$  mm. With regard to the measured temperature values which are not available close to the centerline, according to the temperature profile at  $z = 59.5$  mm for the 3% and 6% cases (Fig. 9 and Fig. 10) and at  $z = 29.5$  mm for the 9% (Fig. 3), there is no rapid increase of the temperature profiles. Therefore, it is postulated that there will be a moderate temperature rise close to the centerline. Such a conclusion can also be further substantiated by the OH profiles (in Fig. 4, 5 and later in Fig. 11).

In Section 4.1, the OH number density distribution for the 3%  $O_2$  and 6%  $O_2$  cases was presented with two different turbulent Schmidt numbers. The OH profile of the 9%  $O_2$  case is shown in Fig. 11 with  $Sc_t = 1.2$ . Slightly under-predicted OH number density levels are shown at axial locations of  $z = 14.5, 22.5$  and  $29.5$  mm. However, a significant over-estimation (approximately four times) can be observed at  $z = 59.5$  mm, different from the 3%  $O_2$  (around two times over-prediction) and 6%  $O_2$  cases (no obvious over-prediction).

Such significant difference in prediction is due to inaccurate prediction of the flame weak-to-strong transition height. This is supported by Fig. 16, where the predicted OH number density profiles and

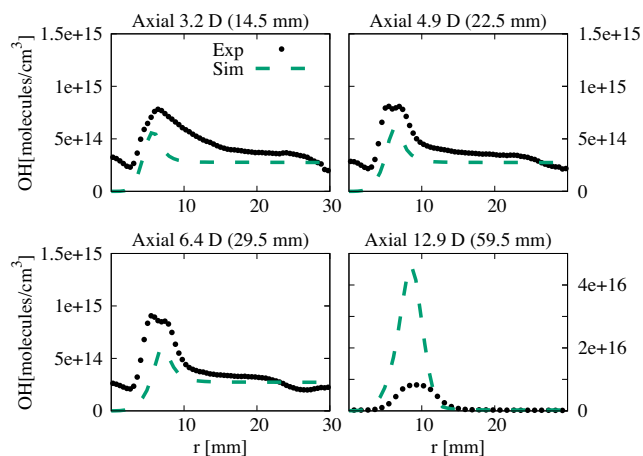


Fig. 11. Mean experimental and numerical OH number density profiles at several axial locations. Coflow oxygen level of 9%.

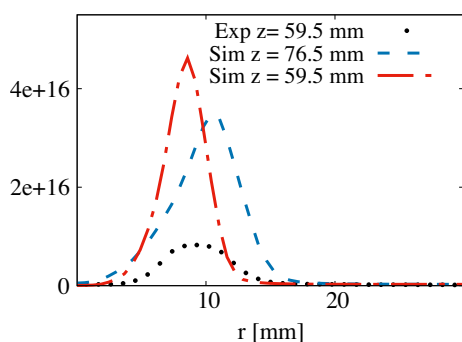


Fig. 12. The predicted OH number density at the locations of  $z = 59.5$  mm and  $z = 76.5$  mm compared to the experimental profile.

experimentally measured OH-LIF instantaneous images are presented. The model predicted a later ignition location. However, the OH level is first increased to a peak value and further decreased. Matching the ignition points of the model to the experimental value leads to a more satisfactory agreement. The predicted ignition location is approximately located at the location of  $z = 42$  mm. While the experimental one, according to the OH-LIF profile in Fig. 16, is located at  $z = 25$  mm. Therefore, the ignition location is over-predicted by around 17 mm with the numerical simulation. As a result, the OH number density at  $z = 59.5 + (42 - 25) = 76.5$  mm from the numerical simulation is compared with the experimental value at  $z = 59.5$  mm in Fig. 11. According to Fig. 12, the over-prediction is alleviated at  $z = 76.5$  mm and the shape of the curve better matches the experimental profile.

In the present *n*-heptane flame, the production of  $\text{CH}_2\text{O}$  is directly linked to the formation of CO (see the chemical pathway presented in the Supplementary material), thus to heat release and flame ignition. The predicted  $\text{CH}_2\text{O}$  levels are compared with the experimentally measured PLIF signals, in Figs. 13–15. Both experimental and numerical  $\text{CH}_2\text{O}$  profiles are normalized between 0 and 1. The location of the peak values, and the general shape, are well predicted. However, the experiments show an increase in signal close to the centerline at all four axial locations, which is not reflected in the CFD calculations. This increase is attributed to fuel- and PAH-LIF in this region, though the extent of interference is not quantified. Nevertheless, the overall comparison of the  $\text{CH}_2\text{O}$  profiles in the reaction zone is encouraging.

#### 4.3. OH distribution

When analyzing the OH distribution for the three flames, a weak-to-strong transition is observed, especially for the 9% case, as shown in

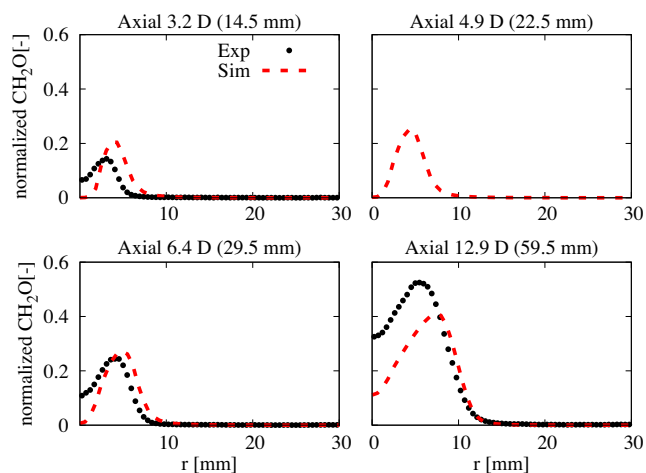


Fig. 13. Mean experimental and numerical normalized  $\text{CH}_2\text{O}$  number density profiles, at different axial locations. Coflow oxygen level of 3%.

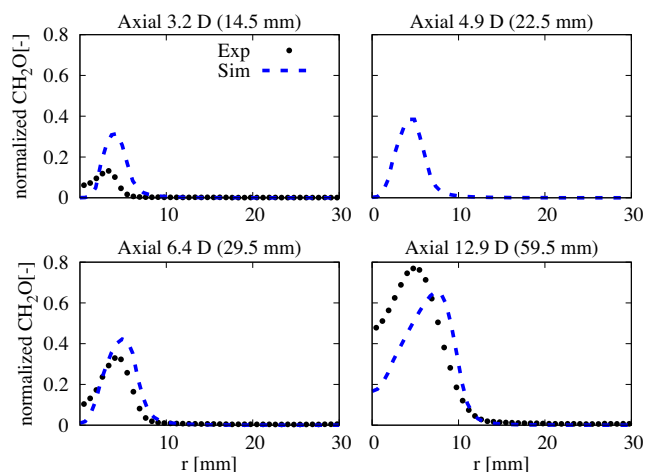


Fig. 14. Mean experimental and numerical normalized  $\text{CH}_2\text{O}$  number density profiles, at different axial locations. Coflow oxygen level of 6%.

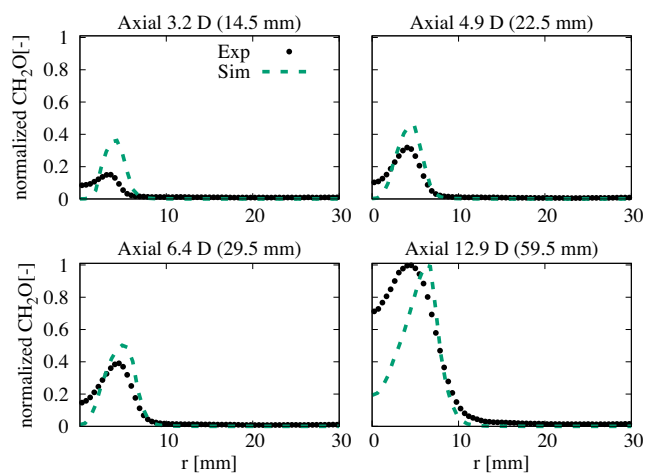
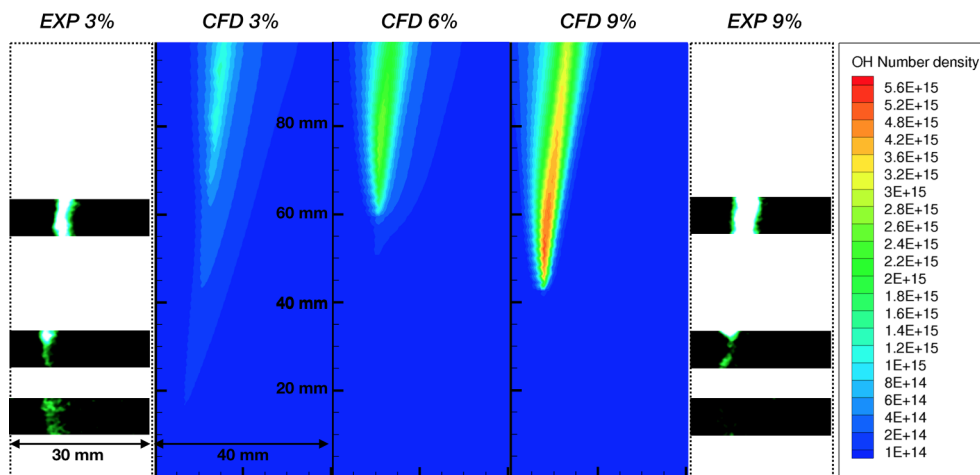
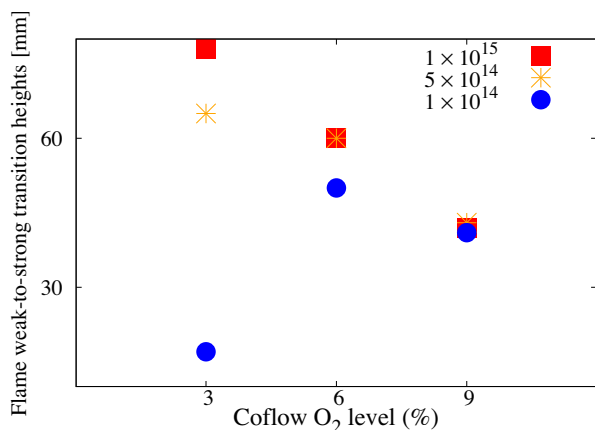


Fig. 15. Mean experimental and numerical normalized  $\text{CH}_2\text{O}$  number density profiles, at different axial locations. Coflow oxygen level of 9%.

Fig. 16, where the modelled OH number density 2D contours are compared with the experimental OH-LIF profiles [8]. The OH-LIF is only available for the 3% and 9% cases. Fig. 16 also indicates the existence of a transitional structure for the 6% case, although not as



**Fig. 16.** Mean OH number density distribution for the 3%, 6% and 9% coflow oxygen levels, compared with the experimental OH-LIF images. The 6% OH-LIF instantaneous image is not available. The threshold OH number density of the numerical contour plot is set to  $10^{14}$  molecules/cm<sup>3</sup>.



**Fig. 17.** Flame weak-to-strong transition heights in mm. The threshold values of  $10^{15}$ ,  $5 \times 10^{14}$  and  $10^{14}$  m, in molecules/cm<sup>3</sup> of OH, are used to identify the flame transition heights.

clearly as for the 3% case. The occurrence of this transitional flame structure was used to indicate the transition away from the MILD combustion regime [10], indicating that none of the cases reach MILD conditions [10,8]. To characterize such behaviour, the “weak-to-strong transition height” is used. From the numerical perspective of view, the definition of such a transition height requires the use of a number density threshold, whose value impacts the transition heights, as indicated in Fig. 17.

When the OH number density threshold value is set to  $10^{15}$  or  $5 \times 10^{14}$  molecules/cm<sup>3</sup>, a monotonic trend relating the flame transition height and coflow oxygen level is observed. Moreover, the transition height for the 3% case is marginally affected by the threshold value. However, the monotonic trend is lost when the threshold value is further reduced to  $10^{14}$  molecules/cm<sup>3</sup>. In this case, the transition height for the 3% coflow oxygen level becomes lower than the other two cases.

Fig. 18 shows the modelled OH streamwise number density gradient distributions from all three cases compared with the experimental flame photographs. If the numerically modelled OH streamwise number density gradient is used to define the flame weak-to-strong heights, there is a non-monotonic trend. Compared to the experimental photographs, the modelled height of the 3% case is in the range of the experimental observed height. For the other two cases, the model predicts slightly higher values of the transition heights. It should be mentioned that the flame weak-to-strong transitional height for the experimental photographs should be estimated by imposing a certain intensity

threshold, indicating the existence of certain uncertainty. However, it is influenced by multiple sources and there is no direct relation to the OH number density or gradient of OH number density.

#### 4.4. Chemical time scale analysis

When the coflow oxygen level is reduced from 9% to 3%, the higher dilution of the fuel-oxidiser mixture reduces the reactivity, and this results in higher values of the characteristic chemical timescale. Fig. 19 shows the chemical timescale distributions for the three cases. The region with chemical timescale longer than 1 s, covering most of the area far away from the centerline, represents the chemically inactive zone. As discussed in Section 2.2, the chemical timescale is evaluated as  $\tau_{c,s} = \frac{Y_{s,s}}{|dY_{s,s}/dt|}$  (s denotes the  $s_{th}$  species in the chemical mechanism, and  $\tau_{c,s}$  is clipped at 1 s). Despite the differences in the width of these regions, the chemical timescales are similar in magnitude for all three cases, for  $z \leq 40$  mm.

Fig. 19 also shows that the active region of the 9% O<sub>2</sub> case tends to expand—and becomes chemically faster (more active) than the other two cases—in the region  $z \geq 45$  mm, with shorter chemical timescales (below 5 ms). On the other hand, the 3% and 6% cases show narrower chemically active zones. With increased oxygen level, the fuel is decomposed faster and the reaction zone is propagated further into the fuel stream [77]. Increased reactivity results in higher heat release rate peak for the 9% O<sub>2</sub>. This matches the high OH number density gradient at around  $z = 40$  mm (Fig. 18, 9% case). The widening of the region of low chemical timescale (high reactivity) for the 6% O<sub>2</sub> is localised at around  $z = 60$  mm (Fig. 19). For the 3% O<sub>2</sub> case, an area with low chemical timescale is visible only after  $z = 80$  mm, showing the reduced reactivity of this case.

Fig. 20 shows line plots with the minimum chemical timescale value along the axial direction. For all the three cases, there exists a slow decrease of chemical time starting from  $z = 0$  mm and a drastic drop at around  $z = 45/60/80$  mm, for 3%/6%/9% coflow levels, respectively. Such observation concurs with the 2D contour plot in Fig. 19.

The contours of chemical timescale distribution for the three oxygen levels show the effect of the increased availability of oxygen on the reactivity of the system. This directly impacts the combustion model via the reacting fraction  $\kappa$ . Furthermore, the analysis of the mixing timescale (shown in Supplementary material) for the three cases indicates very similar distributions regardless of the oxygen level. The same was reported by Evans et al. on C<sub>2</sub>H<sub>4</sub> and CH<sub>4</sub>/H<sub>2</sub> JHC flames with varied coflow oxygen levels [78,79]. Therefore, the chemical time scale becomes the controlling parameter for the determination of  $\kappa$  and the final mean reaction rate,  $\bar{\omega}_s$ .

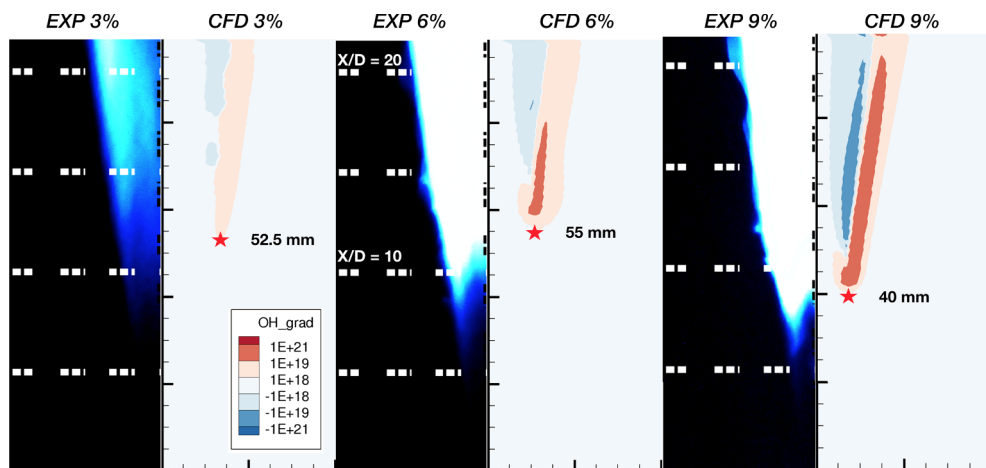


Fig. 18. Mean OH number density stream-wise (axial) gradient distribution for 3%, 6% and 9% coflow oxygen levels compared with the experimental flame photographs taken with an ISO sensitivity of 1600, exposure time of 1/15 s and an f-number of 2 [8]. The star denotes the location of the flame weak-to-strong height. The major and minor ticks represent 20 mm and 5 mm, respectively.

#### 4.5. Investigation on negative heat release rate region

Previous numerical studies on methane by de Joannon and co-workers [44,3] demonstrated the absence of a net negative heat release rate region in MILD combustion, because of the suppression of pyrolytic reactions. Line and contour plots of the heat release rate with three different coflow oxygen levels are presented in Figs. 21 and 22. Both figures show that a negative heat release rate region exists for all the cases. This conclusion agrees with that of Ye et al. [8], who demonstrated the dependence of the net heat release rate profile on strain-rate. Furthermore, studies of laminar opposed-flow flames noted that the net negative heat release rate region only vanished for *n*-heptane in highly diluted conditions (99% N<sub>2</sub> by volume [80]). However, in contrast to this, additional two-dimensional simulations with coflow O<sub>2</sub> concentrations of 1% and 2% (shown in Supplementary material) suggest that the negative heat release rate region still exists if the coflow oxygen level is reduced to 2% and 1% in the numerical simulations (profiles shown in Supplementary material) and the absolute value for negative heat release rate is even higher with lower oxygen content, thus following the trend shown by the 3%, 6% and 9% cases. Moreover, reducing the coflow oxygen level below 3% leads to very weak transitional OH signals.

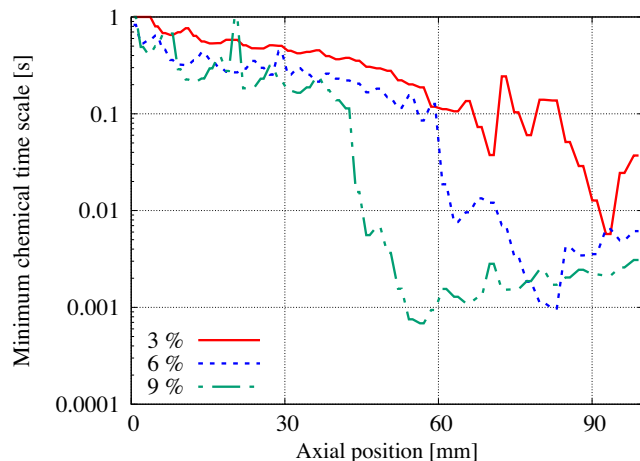


Fig. 20. Minimum chemical timescale values along the axial direction for the cases with 3%, 6% and 9% coflow oxygen levels.

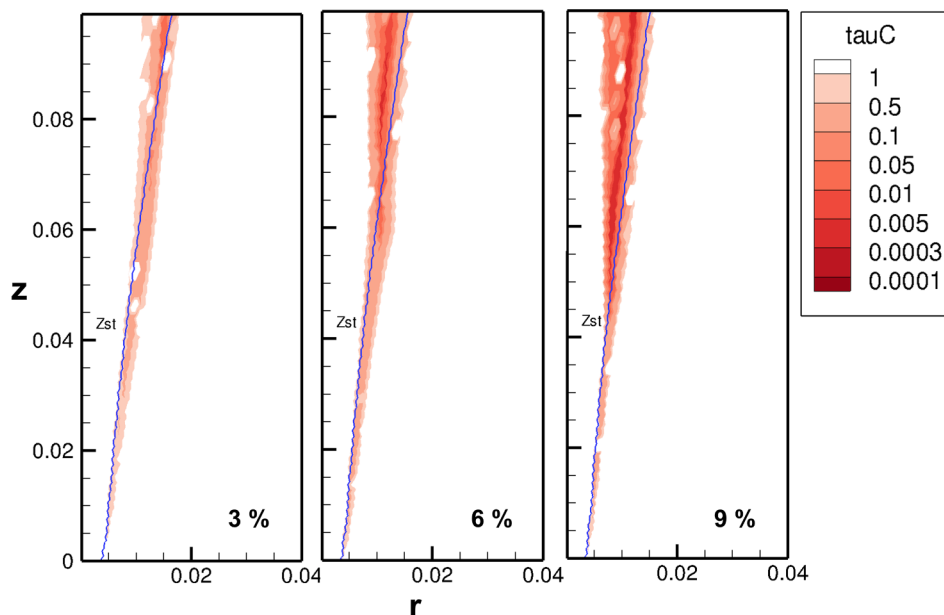
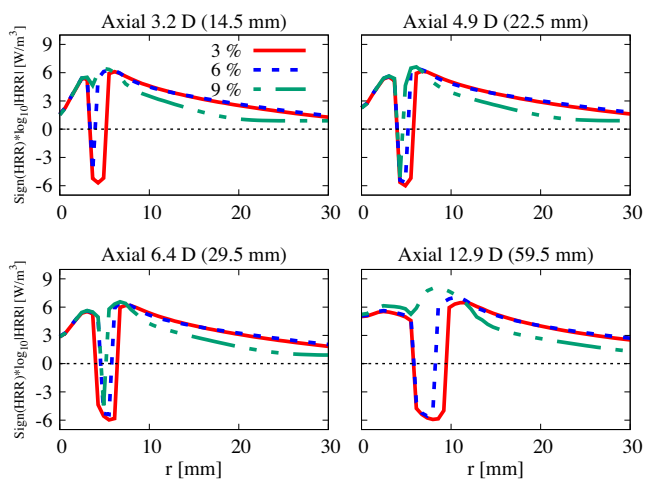


Fig. 19. Chemical timescale distribution for the 3%, 6% and 9% coflow oxygen levels. The active chemical time clipping value is set at 1 s. The isoline of stoichiometric mixture fraction is presented with a solid blue line.



**Fig. 21.** Heat release rate (HRR) for the cases with 3%, 6% and 9% coflow oxygen levels at several axial locations. Note the heat release rates are plotted in logarithmic scale (base 10) and multiplied with the HRR sign.

The influence of strain rate on the net heat release rate in laminar opposed-flow flames was analysed by Ye et al. [8], spanning several orders of magnitude. Their results showed that the 9% O<sub>2</sub> case was always characterised by a larger absolute value of negative heat release rate than the 3% O<sub>2</sub> case. One significant difference between different oxygen dilutions is the trend between the absolute value of negative heat release rate and the strain rate. For the 9% O<sub>2</sub> case, the absolute value of HRR increases monotonically as the strain rate is increased from 80 s<sup>-1</sup> to 320 s<sup>-1</sup>, whereas it decreases monotonically for the 3% O<sub>2</sub> case in the same range.

In Fig. 22, the heat release rate is represented with filled color maps, with superimposed lines of strain rate values and the isoline of stoichiometric mixture fraction. It is shown that the negative heat release rate regions for all the three cases are located in the rich part of the flames. In the 3% O<sub>2</sub> case, a region of negative heat release rate extends along the whole simulation domain, over a wide range of axial strain rates (up to 500 s<sup>-1</sup>), parallel to the positive heat release rate region. In the 6% and 9% O<sub>2</sub> cases, the area of positive heat release rate becomes wider while the net negative region shrinks. The regions of negative heat release rate for the 6% and 9% O<sub>2</sub> cases are located mainly around

the low and medium strain rates. This observation does not concur with the results from Ye et al. [8], who showed that the 9% O<sub>2</sub> tends to have more negative heat release rate when larger strain rate is applied. However, the strain rate from Ye et al. [8] is perpendicular to the flame front direction, while the strain rate discussed in this paper is in the axial direction. Furthermore, the axial and radial strain rate profiles are very similar across all cases (as shown in the [Supplementary material](#)). It is therefore reasonable to conclude that the existence of the negative heat release rate is not dominated by the flow-field, but rather by chemical reactions.

As explained by Ye et al. [8], the negative heat release rate region for the 3% case appears because the *n*-heptane fuel pyrolysis process is not suppressed by the low temperature and low oxygen concentration, it can proceed through alternative paths which are featured by lower activation energy. A detailed discussion concerning the chemical pathway for *n*-heptane low temperature pyrolysis process can be found in the [Supplementary material](#).

It is found that two parent fuel low temperature pyrolysis paths exist to produce C<sub>7</sub>H<sub>5</sub> isomers or alkyl radicals, such as pC<sub>4</sub>H<sub>9</sub> and nC<sub>3</sub>H<sub>7</sub>. Then, through secondary pyrolysis, smaller hydrocarbon molecules such as C<sub>2</sub>H<sub>4</sub> and C<sub>2</sub>H<sub>5</sub> are formed. Fig. 23 presents selected key species involved in *n*-heptane pyrolysis and oxidation. The production of nC<sub>7</sub>H<sub>5</sub> from H atom abstraction is highest close to the burner exit for all the three cases. The H atoms are consumed by O<sub>2</sub> to produce HO<sub>2</sub>, as indicated by the H and HO<sub>2</sub> species distribution and formation rate in Fig. 24. In particular, the amount of H radical close to the jet exit is higher for the 3% case than the other two cases and the regions showing a peak of HO<sub>2</sub> formation rate overlap with the location of high nC<sub>7</sub>H<sub>5</sub> concentration. HO<sub>2</sub> is produced from H via the reaction H + O<sub>2</sub> + N<sub>2</sub> ⇌ HO<sub>2</sub> + N<sub>2</sub>. Moreover, the backward reaction of OH + HO<sub>2</sub> ⇌ O<sub>2</sub> + H<sub>2</sub>O further contributes to the production of HO<sub>2</sub>. According to the investigation of non-premixed methane/hydrogen flames by Evans et al. [81], an increase in the availability O<sub>2</sub> in the coflow promotes the backward reaction rate of OH + HO<sub>2</sub> ⇌ O<sub>2</sub> + H<sub>2</sub>O and the forward rate of 2OH (+M) ⇌ O + H<sub>2</sub>O (+M). Additionally, increasing the available O<sub>2</sub> in these cases decreases the influence of the forward third-body reaction involving N<sub>2</sub>: H + O<sub>2</sub> + N<sub>2</sub> ⇌ HO<sub>2</sub> + N<sub>2</sub> [81].

The distribution of nC<sub>7</sub>H<sub>5</sub> and nC<sub>3</sub>H<sub>7</sub>, close to the burner exit is very similar for all oxygen levels, until z = 60 mm (Figs. 23a and 23b). Above z = 60 mm, the production of nC<sub>7</sub>H<sub>5</sub> and nC<sub>3</sub>H<sub>7</sub> are increased with the elevated level of oxygen in the coflow. Similar observations can be made for C<sub>2</sub>H<sub>5</sub>, which is a product from the secondary fuel

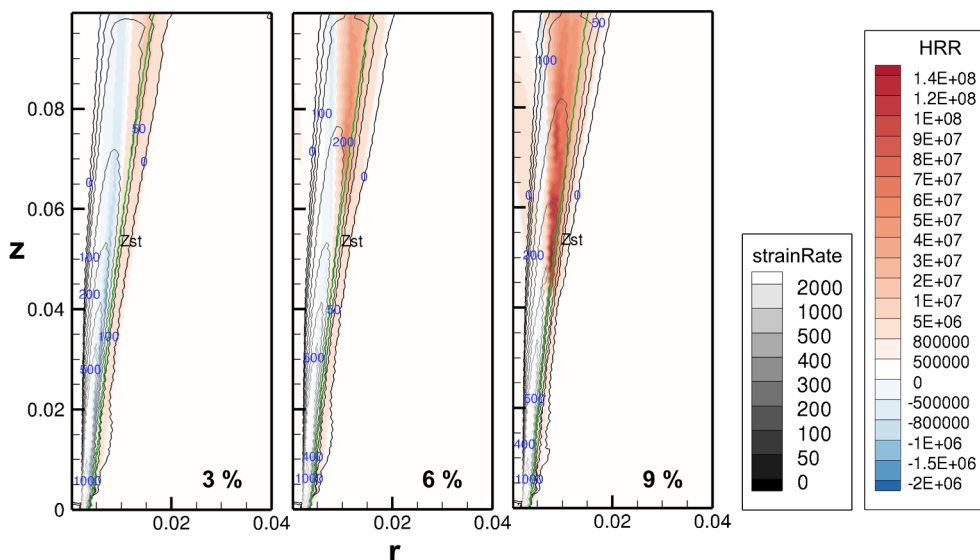


**Fig. 22.** Heat release rate (HRR) for the 3%, 6% and 9% coflow oxygen cases, with superimposed axial strain rate streamlines. The units for strain rate and HRR are s<sup>-1</sup> and W/m<sup>3</sup>, respectively. The isoline of stoichiometric mixture fraction is presented with a solid green line.

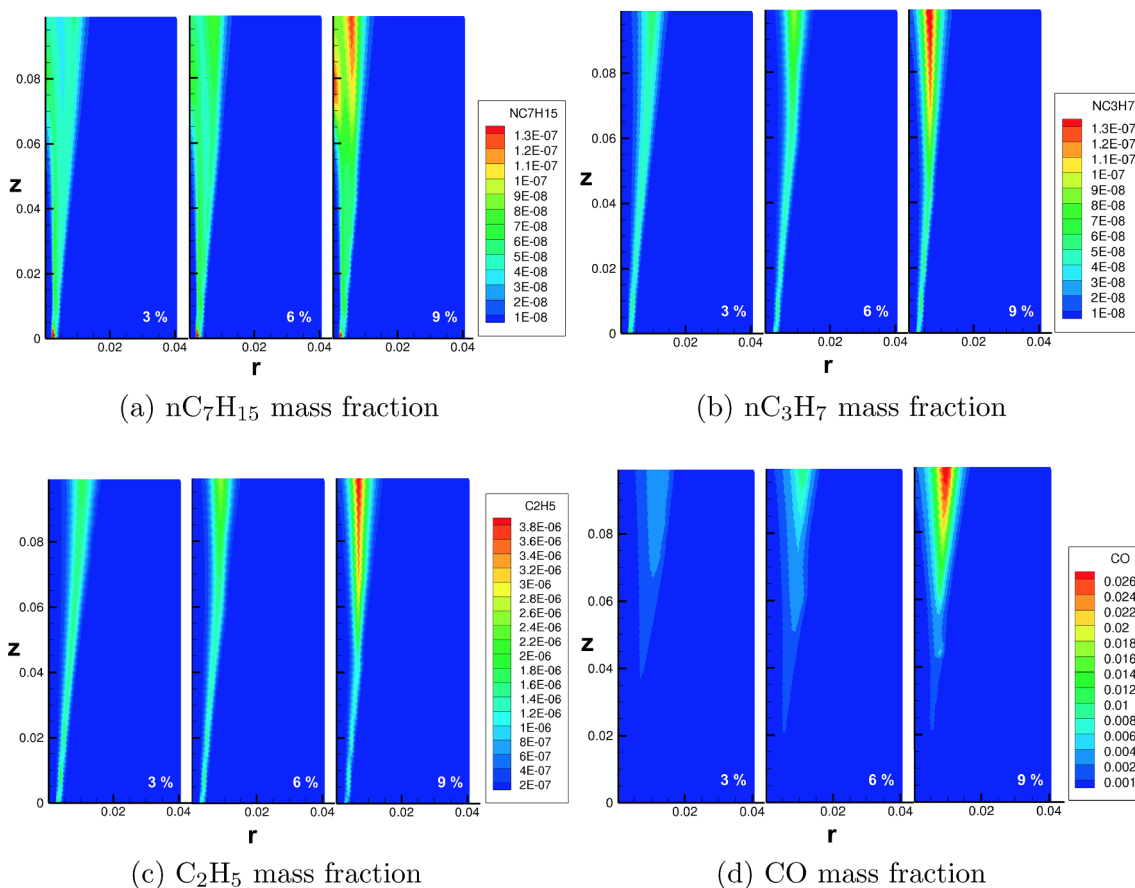


Fig. 23. Mass fractions of species involved in the *n*-heptane chemical pathways for 3%, 6% and 9% coflow oxygen levels.

pyrolysis (Fig. 23c). When the temperature is low, the endothermic reactions are not suppressed for the lower oxygen level cases, as occurs with simple fuels under MILD condition [44,3], because of the existence of multi-path pyrolysis processes. Moreover, the production of CO is quite low, especially upstream (see Fig. 23d). The oxidation of CO to CO<sub>2</sub> results in the largest positive heat release rate. Without the heat release from CO<sub>2</sub> formation, the negative heat release rate due to pyrolytic processes cannot be compensated, resulting in the observed higher absolute values of the negative heat release rate region for the lower coflow oxygen levels.

## 5. Conclusions

Unsteady RANS simulations were carried out, for the first time, to investigate the characteristics of the *n*-heptane turbulent flames in a jet-in-hot-coflow (JHC) burner. The PaSR combustion model was used with detailed chemistry and a dynamic evaluation of the mixing timescale. The simulations were used to support the interpretation of newly available experimental data from laser-based diagnostics. The use of unsteady RANS with reactor-based models and detailed chemistry offers a number of insights which can be summarized as:

- A turbulent Schmidt number of 1.2 and the use of the Pope correction for the jet spreading rate provide the most satisfactory predictions on mean temperature, OH number density and CH<sub>2</sub>O signal. The turbulent Schmidt number used in the present work helps decreasing the turbulent diffusivity of the chemical species, retarding ignition in agreement with the experimental observations.
- The numerically modelled flame weak-to-strong transition height depends on the threshold value used for the OH number density. For

threshold values above  $5 \times 10^{14}$  molecules/cm<sup>3</sup>, a monotonic decreasing trend is observed as a function of the oxygen level in the coflow. However, such observation is not valid when the threshold OH number density value is further reduced to  $10^{14}$  molecules/cm<sup>3</sup>. In this case, a non-monotonic trend between flame weak-to-strong height and the coflow oxygen level is captured. The predicted flame weak-to-strong transition heights based on the streamwise gradient of OH number density show a non-monotonic behaviour as well. Therefore, changing the threshold of OH number density value or the definition of flame weak-to-strong transition height can affect the interpretation of the predicted trend for flame transition height, hence impacting the classification of the flame.

–A transitional flame structure can be observed for the 3% O<sub>2</sub> case, based on the distribution of OH number density (threshold set to  $10^{14}$  molecules/cm<sup>3</sup>), and on the chemical timescale distribution. This is in agreement with the experimental findings.

–Two chemical pathways in *n*-heptane allow an alternative pyrolysis path with lower activation energy in low temperature and low oxygen conditions. This leads to an expanded negative heat release rate region as the coflow oxygen level decreases, which is not associated to a specific range of strain rates. Such observation indicates that none of the three coflow oxygen level cases reach fully MILD condition.

In summary, it is more difficult to achieve MILD combustion using *n*-heptane than with the simple fuels like methane and ethylene. Due to the existence of two pyrolysis chemical pathways, the appearance of the transitional structure in *n*-heptane flames happens at lower coflow oxygen level compared to simple fuels.

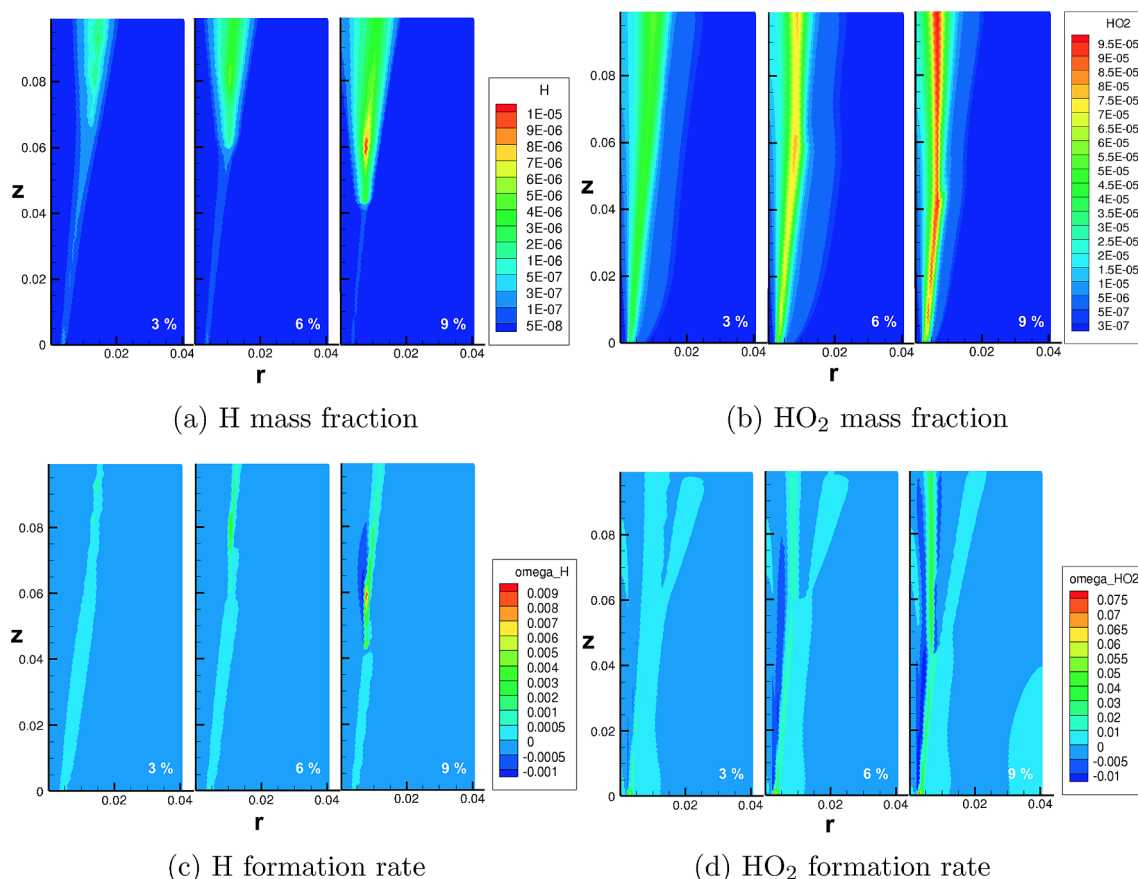


Fig. 24. Mass fractions and formation rates of H and HO<sub>2</sub> for 3%, 6% and 9% coflow oxygen levels.

#### CRedit authorship contribution statement

**Zhiyi Li:** Conceptualization, Methodology, Validation, Investigation, Visualization, Writing - original draft. **Michael J. Evans:** Conceptualization, Investigation, Writing - review & editing. **Jingjing Ye:** Conceptualization, Investigation. **Paul R. Medwell:** Conceptualization, Supervision, Writing - review & editing. **Alessandro Parente:** Conceptualization, Supervision, Writing - review & editing.

#### Declaration of Competing Interest

The authors declare that they have no known competing financial interests or personal relationships that could have appeared to influence the work reported in this paper.

#### Acknowledgement

This project has received funding from the European Union's Horizon 2020 research and innovation program under the Marie Skłodowska-Curie grant agreement No. 643134; the European Research Council, Starting Grant No. 714605; the Australian Research Council (ARC) through the Discovery (DP and DECRA) programme; the United States Air Force Asian Office of Aerospace Research and Development (AOARD) and the China Scholarship Council.

#### Appendix A. Supplementary data

Supplementary data associated with this article can be found, in the online version, at <https://doi.org/10.1016/j.fuel.2020.118748>.

#### References

- [1] Wüning JA, Wüning JG. Flameless oxidation to reduce thermal NO-formation. *Prog Energy Combust Sci* 1997;23:81–94.
- [2] Cavaliere A, de Joannon M. MILD combustion. *Prog Energy Combust Sci* 2004;30:329–66.
- [3] de Joannon M, Sorrentino G, Cavaliere A. MILD combustion in diffusion-controlled regimes of hot diluted fuel. *Combust Flame* 2012;159:1832–9.
- [4] Parente A, Malik MR, Contino F, Cuoci A, Dally BB. Extension of the Eddy Dissipation Concept for turbulence/chemistry interactions to MILD combustion. *Fuel* 2015;163:98–111.
- [5] Oldenhof E, Tummers MJ, van Veen E, Roekaerts D. Ignition kernel formation and lift-off behaviour of Jet-in-Hot-Coflow flames. *Combust Flame* 2010;157:1167–78.
- [6] Dally BB, Karpets AN, Barlow RS. Structure of turbulent non-premixed jet flames in a diluted hot coflow. *Proc Combust Inst* 2002;29:1147–54.
- [7] Kalt P, Dally B. The effect of jet preheating on turbulence in a premixed jet in hot coflow. In: *Proceedings of the Australian Combustion Symposium*.
- [8] Ye J, Medwell PR, Evans MJ, Dally BB. Characteristics of turbulent n-heptane jet flames in a hot and diluted coflow. *Combust Flame* 2017;183:330–42.
- [9] Medwell PR, Dally BB. Effect of fuel composition on jet flames in a heated and diluted oxidant stream. *Combust Flame* 2012;159:3138–45.
- [10] Evans MJ, Medwell PR, Tian ZF. Modelling lifted jet flames in a heated coflow using an optimised Eddy Dissipation Concept model. *Combust Sci Technol* 2015;187(7):1093–109.
- [11] Oldenhof E, Tummers MJ, van Veen EH, Roekaerts DJEM. Role of entrainment in the stabilisation region of Jet-in-Hot-Coflow flames. *Combust Flame* 2011;158(8):1553–63.
- [12] De A, Oldenhof E, Sathiah P, Roekaerts D. Numerical simulation of Delft-Jet-in-Hot-Coflow (DJHC) flames using the Eddy Dissipation Concept model for turbulence-chemistry interaction. *Flow Turbulence Combustion* 2011;87:537–67.
- [13] Ihme M, See YC. Prediction of autoignition in a lifted methane/air flame using an unsteady flamelet/progress variable mode. *Combust Flame* 2010;157:1850–62.
- [14] Li Z, Cuoci A, Sadiki A, Parente A. Comprehensive numerical study of the Adelaide Jet in Hot-Coflow burner by means of RANS and detailed chemistry. *Energy* 2017;139:555–70.
- [15] Gordon RL, Masri AR, Mastorakos E. Simultaneous rayleigh temperature, oh- and ch2o-lif imaging of methane jets in a vitiated coflow. *Combust Flame* 2008;155:181–95.
- [16] Medwell PR, Kalt PA, Dally BB. Imaging of diluted turbulent ethylene flames stabilized on a Jet in Hot Coflow (JHC) burner. *Combust Flame* 2007;152:100–13.
- [17] Ye J, Medwell PR, Evans MJ, Dally BB. The impact of carrier gas on ethanol flame

- behaviour in a Jet in Hot Coflow (JHC) burner. The Australian Combustion Symposium 2015.
- [18] Ye J, Medwell PR, Dally BB, Evans MJ. The transition of ethanol flames from conventional to MILD combustion. *Combust Flame* 2016;171:173–84.
- [19] Walters EM. Stability and liftoff of non-premixed large hydrocarbon flames in mild conditions [Master's thesis]. Oregon State University; 2017.
- [20] Ye J, Medwell PR, Kleinheinz K, Evans MJ, Dally BB, Pitsch HG. Structural differences of ethanol and dme jet flames in a hot diluted coflow. *Combust Flame* 2018;192:473–94.
- [21] Kruse S, Ye J, Sun Z, Attili A, Dally B, Medwell P, Pitsch H. Experimental investigation of soot evolution in a turbulent non-premixed prevaporized toluene flame. In: *Proceedings of the Combustion Institute*.
- [22] Evans MJ, Medwell PR, Sun Z, Chinnici A, Ye J, Chan QN, Dally BB. Downstream evolution of n-heptane/toluene flames in hot and vitiated coflows. *Combust Flame* 2019;202:78–89.
- [23] Medwell PR, Dally BB. Effect of fuel composition on jet flames in a heated and diluted oxidant stream. *Combust Flame* 2012;159(10):3138–45.
- [24] Ye J, Medwell PR, Varea E, Kruse S, Dally BB, Pitsch HG. An experimental study on mild combustion of prevaporised liquid fuels. *Appl Energy* 2015;151:93–101.
- [25] Weber R, Smart JP, Kamp W. On the (MILD) combustion of gaseous, liquid, and solid fuels in high temperature preheated air. *Proc Combust Inst* 2005;30(2):2623–9.
- [26] Reddy VM, Biswas P, Garg P, Kumar S. Combustion characteristics of biodiesel fuel in high recirculation conditions. *Fuel Process Technol* 2014;118:310–7.
- [27] Sidey J, Mastorakos E, Gordon RL. Simulations of autoignition and laminar pre-mixed flames in methane/air mixtures diluted with hot products. *Combust Sci Technol* 2014;186(4–5):453–65. <https://doi.org/10.1080/00102202.2014.883217>.
- [28] Medwell P, Kalt P, Dally B. Imaging of diluted turbulent ethylene flames stabilized on a jet in hot coflow (jhc) burner. *Combust Flame* 2008;152(1):100–13.
- [29] Christo FC, Dally BB. Modelling turbulent reacting jets issuing into a hot and diluted coflow. *Combust Flame* 2005;142:117–29.
- [30] Gordon RL, Masri AR, Pope SB, Goldin GM. Transport budgets in turbulent lifted flames of methane autoigniting in a vitiated co-flow. *Combust Flame* 2007;151(3):495–511.
- [31] Frassoldati A, Sharma P, Cuoci A, Faravelli T, Ranzi E. Kinetic and fluid dynamics modeling of methane/hydrogen jet flames in diluted coflow. *Appl Therm Eng* 2009;30:376–83.
- [32] Mardani A, Tabejamaat S, Ghamari M. Numerical study of influence of molecular diffusion in the MILD combustion regime. *Combust Theor Model* 2010;14(5):747–74.
- [33] Shababian SR, Medwell PR, Rahimi M, Frassoldati A, Cuoci A. Kinetic and fluid dynamic modeling of ethylene jet flames in diluted and heated oxidant stream combustion conditions. *Appl Therm Eng* 2012;52:538–54.
- [34] Aminian J, Galletti C, Tognotti L. Extended EDC local extinction model accounting finite-rate chemistry for MILD combustion. *Fuel* 2016;165:123–33.
- [35] Mardani A. Optimization of the Eddy Dissipation Concept (EDC) model for turbulence-chemistry interactions under hot diluted combustion of ch4/h2. *Fuel* 2017;191:114–29.
- [36] Evans M, Chinnici A, Medwell P, Ye J. Ignition features of methane and ethylene fuel-blends in hot and diluted coflows. *Fuel* 2017;203:279–89.
- [37] Chen Z, Reddy V, Ruan S, Doan N, Roberts W, Swaminathan N. Simulation of MILD combustion using perfectly stirred reactor model. *Proc Combust Inst* 2017;36(3):4279–86.
- [38] Li Z, Ferrarotti M, Cuoci A, Parente A. Finite-rate chemistry modelling of non-conventional combustion regimes using a partially-stirred reactor closure: Combustion model formulation and implementation details. *Appl Energy* 2018;225:637–55.
- [39] Ihme M, See YC. LES flamelet modeling of a three-stream MILD combustor: analysis of flame sensitivity to scalar inflow conditions. *Proceeding of the Combustion Institute* 2011;33(1):1309–17.
- [40] Ihme M, Zhang J, He G, Dally B. Large Eddy Simulation of a Jet-in-Hot-Coflow burner operating in the oxygen-diluted combustion regime. *Flow Turbulence Combust* 2012;89:449–64.
- [41] Domingo P, Vervisch L, Veynante D. Large-eddy simulation of a lifted methane jet flame in a vitiated coflow. *Combust Flame* 2008;152(3):415–32.
- [42] Li Z, Cuoci A, Parente A. Large eddy simulation of mild combustion using finite rate chemistry: effect of combustion sub-grid closure. *Proc Combust Inst* 2019;37:4519–29.
- [43] Yoo CS, Richardson ES, Sankaran R, Chen JH. A dns study on the stabilization mechanism of a turbulent lifted ethylene jet flame in highly-heated coflow. *Proc Combust Inst* 2011;33(1):1619–27.
- [44] de Joannon M, Sabia P, Sorrentino G, Cavaliere A. Numerical study of mild combustion in hot diluted diffusion ignition (hddi) regime. *Proc Combust Inst* 2009;32(2):3147–54.
- [45] Saha M, Dally BB, Medwell PR, Cleary EM. Moderate or Intense Low oxygen Dilution (MILD) combustion characteristics of pulverized coal in a self-re recuperative furnace. *Energy Fuels* 2014;28(9):6046–57. <https://doi.org/10.1021/ef5006836>.
- [46] Ye J, Medwell PR, Varea E, Kruse S, Dally BB, Pitsch HG. An experimental study on MILD combustion of prevaporised liquid fuels. *Appl Energy* 2015;151:93–101.
- [47] Minamoto Y, Swaminathan N. Subgrid scale modelling for MILD combustion. *Proc Combust Inst* 2015;35(3):3529–36.
- [48] Magnussen BF. On the structure of turbulence and a generalized Eddy Dissipation Concept for chemical reaction in turbulent flow. In: 19<sup>th</sup> AIAA Aerospace Science Meeting, St. Louis, Missouri, USA; 1981.
- [49] Gran I, Magnussen BF. A numerical study of a bluff-body stabilized diffusion flame, part 2: influence of combustion modelling and finite-rate chemistry. *Combust Sci Technol* 1996;119(1–6):191–217.
- [50] Magnussen BF. The Eddy Dissipation Concept a bridge between science and technology. In: *ECCOMAS Thematic Conference on Computational Combustion*, Lisbon, Portugal; 2005.
- [51] Chomiak J. *Combustion: A Study in Theory, Fact and Application*. Abacus Press/Gorden and Breach Science Publishers; 1990.
- [52] Peters N. *Turbulent Combustion*. Cambridge University Press; 2000.
- [53] Magnussen B, Hjertager B. On mathematical modeling of turbulent combustion with special emphasis on soot formation and combustion. *Symp (Int) Combust* 1977;16(1):719–29.
- [54] Ferrarotti M, Li Z, Parente A. On the role of mixing models in the simulation of MILD combustion using finite-rate chemistry combustion models. *Proceeding of the Combustion Institute* 2018;000:1–8.
- [55] Li Z, Ferrarotti M, Cuoci A, Parente A. Finite-rate chemistry modelling of non-conventional combustion regimes using a partially-stirred reactor closure: combustion model formulation and implementation details. *Appl Energy* 2018;225:637–55.
- [56] Lysenko DA, Ertesvåg IS, Rian KE. Numerical simulation of non-premixed turbulent combustion using the Eddy Dissipation Concept and comparing with the steady laminar flamelet model. *Flow Turbulence Combust* 2014;53:577–605.
- [57] Pope SB. *An explanation of the turbulent round-jet/plane-jet anomaly*. Imperial College London; 1978. Tech. rep.
- [58] Golovitchev V, Chomiak J. Numerical modeling of high temperature air flameless combustion, in: *The 4th international symposium on high temperature air combustion and gasification*. 2001.
- [59] Kärholm FP. Numerical modelling of diesel spray injection, turbulence interaction and combustion [Ph.d. thesis]. Chalmers, Sweden: Chalmers University of Technology; 2008.
- [60] Raman V, Pitsch H. A consistent LES/filtered-density function formulation for the simulation of turbulent flames with detailed chemistry. *Proc Combust Inst* 2007;31(2):1711–9.
- [61] Ye I. Investigation of the scalar variance and scalar dissipation rate in urans and les [Ph.d. thesis]. Ontario, Canada, Waterloo, Ontario, Canada: University of Waterloo; 2011.
- [62] Sanders JPH, Gökalp I. Scalar dissipation rate modelling in variable density turbulent axisymmetric jets and diffusion flames. *Phys Fluids* 1998;10(4):938–48.
- [63] Isaac BJ, Parente A, Galletti C, Thornock JN, Smith PJ, Tognotti L. A novel methodology for chemical time scale evaluation with detailed chemical reaction kinetic. *Energy Fuels* 2013;27(4):2255–65.
- [64] Fox RO. *Computational Models for Turbulent Reacting Flows*. Cambridge, UK: Cambridge University Press; 2003.
- [65] Chomiak J, Karlsson A. Flame liftoff in diesel sprays. In: *Twenty-Sixth Symposium (International) on Combustion*, The Combustion Institute; 1996. p. 2557–564.
- [66] Sutton JA, Williams BA, Fleming JW. Laser-induced fluorescence measurements of ncn in low-pressure ch4/o2/n2 flames and its role in prompt no formation. *Combust Flame* 2008;153(3):465–78.
- [67] Medwell PR. Laser diagnostics in mild combustion [Ph.d. thesis]. Adelaide, Australia: University of Adelaide; 2007.
- [68] Longo R, Frst M, Bellemans A, Ferrarotti M, Derudi M, Parente A. Cfd dispersion study based on a variable schmidt formulation for flows around different configurations of ground-mounted buildings. *Build. Environ*.
- [69] Medwell PR, Blunck DL, Dally BB. The role of precursors on the stabilisation of jet flames issuing into a hot environment. *Combust Flame* 2014;161(2):465–74.
- [70] Medwell PR, Evans MJ, Chan QN, Katta VR. Laminar flame calculations for analyzing trends in autoignitive jet flames in a hot and vitiated coflow. *Energy Fuels* 2016;30:8680–90.
- [71] Evans M, Chinnici A, Medwell P, Ye J. Ignition features of methane and ethylene fuel-blends in hot and diluted coflows. *Fuel* 2017;203:279–89.
- [72] Ranzi E, Frassoldati A, Stagni A, Pelucchi M, Cuoci A, Faravelli T. Reduced kinetic schemes of complex reaction systems: Fossil and biomass-derived transportation fuels. *Int J Chem Kinet* 2014;46(9):512–42.
- [73] Stagni A, Cuoci A, Frassoldati A, Faravelli T, Ranzi E. Lumping and reduction of detailed kinetic schemes: an effective coupling. *Ind Eng Chem Res* 2014;53(22):9004–16.
- [74] Stagni A, Frassoldati A, Cuoci A, Faravelli T, Ranzi E. Skeletal mechanism reduction through species-targeted sensitivity analysis. *Combust Flame* 2016;163:382–93.
- [75] Mehl M, Pitz WJ, Westbrook CK, Curran HJ. Kinetic modeling of gasoline surrogate components and mixtures under engine conditions. *Proc Combust Inst* 2011;33(1):193–200.
- [76] Curran H, Gaffuri P, Pitz W, Westbrook C. A comprehensive modeling study of n-heptane oxidation. *Combust Flame* 1998;114(1):149–77.
- [77] Evans M, Petre C, Medwell P, Parente A. Generalisation of the eddy-dissipation concept for jet flames with low turbulence and low damkholder number. *Proc Combust Inst* 2019;37(4):4497–505.
- [78] Evans M, Medwell P, Wu H, Stagni A, Ihme M. Classification and lift-off height prediction of non-premixed mild and autoignitive flames. *Proc Combust Inst* 2017;36(3):4297–304.
- [79] Evans M, Petre C, Medwell P, Parente A. Generalisation of the eddy-dissipation concept for jet flames with low turbulence and low damkholder number. In: *Proceedings of the Combustion Institute*.
- [80] de Joannon M, Sabia P, Cavaliere A. Alternative ignition systems, Tech. Rep. 133–150, Verlag ProcessEng Engineering GmbH.
- [81] Evans MJ, Medwell PR, Tian ZF, Ye J, Frassoldati A, Cuoci A. Effects of oxidant stream composition on non-premixed laminar flames with heated and diluted coflows. *Combust Flame* 2017;178:297–310.